ADVANCED MATERIALS INTERFACES

www.advmatinterfaces.de

Atomic Structure and Chemistry of Self-Assembled Nanopillar Composite Oxides

*Xiumei Ma, Zhaoliang Liao, Lin Li, and Peng Gao**

Artificial engineered thin films consisting of $(LaSr)(MnV)O_3$ matrix and columnar nanocomposites oxides are deposited on single-crystal $LaAlO_3$ (111) substrates by using $La_{2/3}Sr_{1/3}MnO_3$ and V_2O_3 targets. The epitaxial grown $(LaSr)(MnV)O_3$ thin-film matrix is embedded with self-assembled MnO and V_2O_3 columns with a few nanometers in size. The atomic structure, chemistry, and electronic properties of columnar nanocomposite are determined and the bonding between the matrix and nanopillars is identified by using atomically resolved scanning transmission electron microscopy and electron energy loss spectroscopy.

1. Introduction

Complex transition metal oxides (TMOs) are strongly correlated electronic materials, in which the spin, charge, orbital, and lattice are simultaneously active and competitive.[1] Many novel physical properties, such as colossal magnetoresistance,[2] charge ordering,[3] electronic phase separation,[4] and metal–insulator transition,[5] have been reported in the TMOs. The epitaxial composite TMOs thin films can be fabricated in either horizontal form with multilayers[6–9] or vertical form with columnar nanocomposites.[10–16] In fact, the columnar nanocomposites geometry provides numerous advantages over the form of horizontal multilayers, e.g., intrinsic heteroepitaxy in three dimensions and a larger interfacial area. These columnar nanocomposites with vertical interfaces and nanoscale phase separation can serve as superstructures and the interplays may also occur between the nanoscale phases. The columnar nanocomposites also offer more variables for tuning the properties. Besides the substrate strain engineering, the functionalities of nanocomposites can be controlled by the phase ratio, phase size, and the relative orientations between the phases.

Dr. X. Ma, Prof. P. Gao
Electron Microscopy Laboratory
School of Physics
Peking University
Beijing 100871, China
E-mail: p-gao@pku.edu.cn
Dr. Z. Liao, Dr. L. Li
Department of Physics and Astronomy
Louisiana State University
Baton Rouge, LA 70810, USA
Prof. P. Gao
Collaborative Innovation Center of Quantum Matter
Beijing 100871, China

DOI: 10.1002/admi.201700225

In the past few years, many nanocomposites thin films have been achieved by the advanced metal-organic aerosol deposition or pulsed laser deposition (PLD) technique, such as $BaTiO_3$–$CoFe_2O_4$,[17] $(La_{0.7}Sr_{0.3}MnO_3)_{1-x}$:$(MgO)_x$,[18] $(La_{0.7}Ca_{0.3}MnO_3)_{1-x}$:$(MgO)_x$,[19] and $(La_{0.7}Sr_{0.3}MnO_3)_{0.5}$:$(ZnO)_{0.5}$ nanocomposites.[20] For example, tunable metal–insulator transition has been realized previously in $La_{2/3}Sr_{1/3}MnO_3$ (LSMO)–V_2O_3 nanocomposites by engineering the relative chemical ratio between LSMO and V_2O_3 during PLD growth.[21]

The functionalities of the nanocomposites film are determined by the structure and chemistry of nanoscale phases and the interfaces between them. The interfaces can have a strong impact on the lattice distortion, spin-orbital-charge coupling and electron scattering, and thus finally generate novel phenomena as occurring in the planar heterostructures.[22,23] Therefore, the investigations on the nanoscale structures and their interfaces, chemistry, and electronic structures are crucial for not only revealing the mechanism of nanocomposite formation but also understanding the underlying structure–property relation, which consequently will guide us the control of nanocomposite growth and as a result the functionality engineering for device applications. However, the buried interfaces in nanocomposites are usually diffuse, rough, and/or heterogeneous,[24–26] making it very difficult to extract the atomic bonding information and chemistry of interfaces.

In this paper, we study the microstructure of nanocomposite $(LaSr)(MnV)O_3$ (LSMVO) thin films using the aberration-corrected scanning transmission electron microscopy (Cs-STEM) and electron energy loss spectroscopy (EELS). We find that the epitaxial grown LSMVO thin-film matrix is embedded with two types of self-assembled columnar composite oxides, i.e., MnO and V_2O_3 nanopillars. The structure and composition of these nanopillars are identified. The atomic bonding and electronic structures at the heterointerfaces of LSMVO/MnO and LSMVO/V_2O_3 are determined. Our findings provide deep insights into the growth mechanism of the nanocomposite and the understanding of the structure driven novel transport properties in these films.

2. Results and Discussion

The detailed structures of nanocomposite thin films have been investigated from both the planar view and cross-sectional view

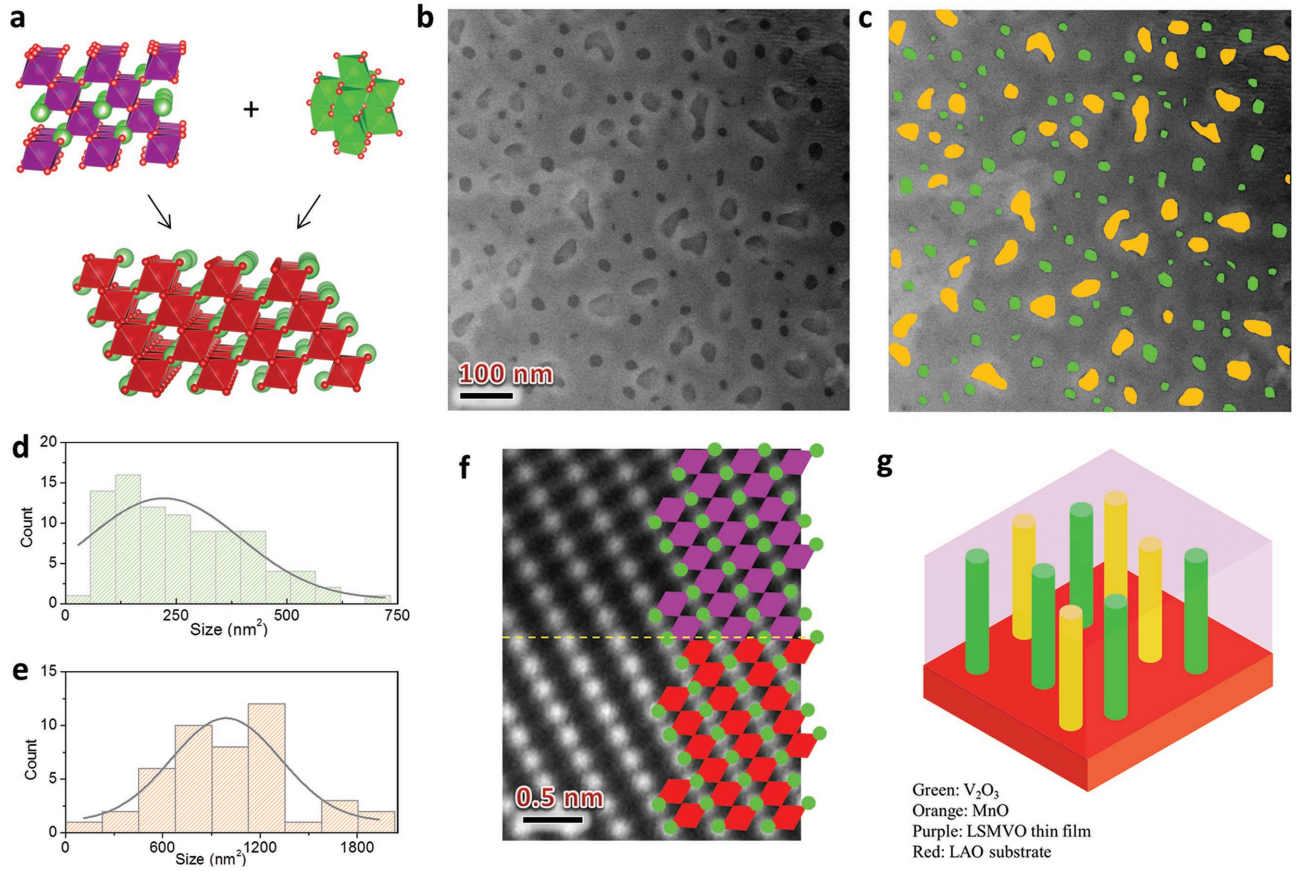

Figure 1. Self-assembled nanopillar thin films. a) A schematic illustration showing the growth of nanostructured thin films on (111)-$LaAlO_3$ substrate by using $La_{2/3}Sr_{1/3}MnO_3$ and V_2O_3 targets. b) STEM image of a planar view of nanostructured thin film showing the self-assembled nanostructures. Two types of nanopillars are observed with gray and dark contrast, respectively. The gray nanopillars are typically elongated, relatively large in size and have bright edges, while the dark nanopillars are circular, small in size. c) Nanopillars are mapped in color. Orange: gray nanopillar (MnO). Green: dark nanopillar (V_2O_3). d) Size (area) distribution of V_2O_3 nanopillars. The area is calculated by Image J software. The size distribution is fitted with Gaussian function. e) Size (area) distribution of MnO nanopillars. The size distribution is fitted with Gaussian function. f) High-resolution Scanning TEM (STEM) image from a cross-sectional view of nanostructured thin films showing the interface of $LaAlO_3$ and (LaSr)(MnV)O_3 matrix. Right inset: a schematic overlaid with the STEM image. g) Schematic illustration of a self-assembled nanopillars in the thin film. Red: perovskite $LaAlO_3$ substrate. Purple: perovskite (LaSr)(MnV)O_3 thin-film matrix. Orange: MnO nanopillars. Green: V_2O_3 nanopillars.

specimens in **Figure 1**. A planar view high-angle annular dark field (HAADF) STEM image of thin film in Figure 1b displays that columnar nanopillars are embedded in a matrix. Two types of nanopillars with gray and dark contrast are observed, respectively. The gray nanopillars are typically elongated, relatively large in size and have bright edges, while the dark nanopillars are circular and small in size. Note that in the HAADF (Z-contrast, Z is atomic number) image, the contrast itself contains the chemical information, i.e., bright usually means larger Z while dark corresponds to a lighter composite. From the later characterization of chemical composition from EELS, the large and gray nanopillars are identified as MnO and the small and dark nanopillars are V_2O_3. In order to clarify the spatial distribution of the nanopillars, MnO and V_2O_3 nanopillars are marked with orange and green in Figure 1c, respectively. The size (area) distributions of V_2O_3 and MnO nanopillars are presented in Figure 1d,e. The area is calculated by ImageJ software and the size distribution is fitted with the Gaussian function. The average areas of MnO and V_2O_3 pillars are ≈1000 and ≈220 nm^2, respectively.

The cross-sectional view specimen reveals a pillar–matrix structure as well and the film thickness is about 25 nm, as shown in Figure S2 (Supporting Information). The nanopillars are formed from the bottom $LaAlO_3$ (LAO) interface to the top of the film. The atomically resolved HAADF STEM image from a cross-sectional view of nanostructured thin films in Figure 1f demonstrates that the LSMVO thin-film matrix was epitaxially grown on the LAO substrate. From the Z-contrast image, the orientation relationship between LSMVO thin-film matrix and the LAO substrate is $(111)_p$-LSMVO//$(111)_p$-LAO (subscript p denotes pseudocubic structure). The bonding between the LSMVO and substrate can also be determined directly as shown by the schematic octahedrons overlaid with the STEM image in the right inset. Figure 1g shows a schematic illustration of self-assembled nanopillars embedded in the perovskite LSMVO thin-film matrix. The MnO (orange) and V_2O_3 (green) nanopillar composite oxides distribute disorderly in the LSMVO thin-film matrix (purple) on the LAO substrate (red).

To further determine the chemical compositions and electronic structures of these two types of nanopillars, the spatial

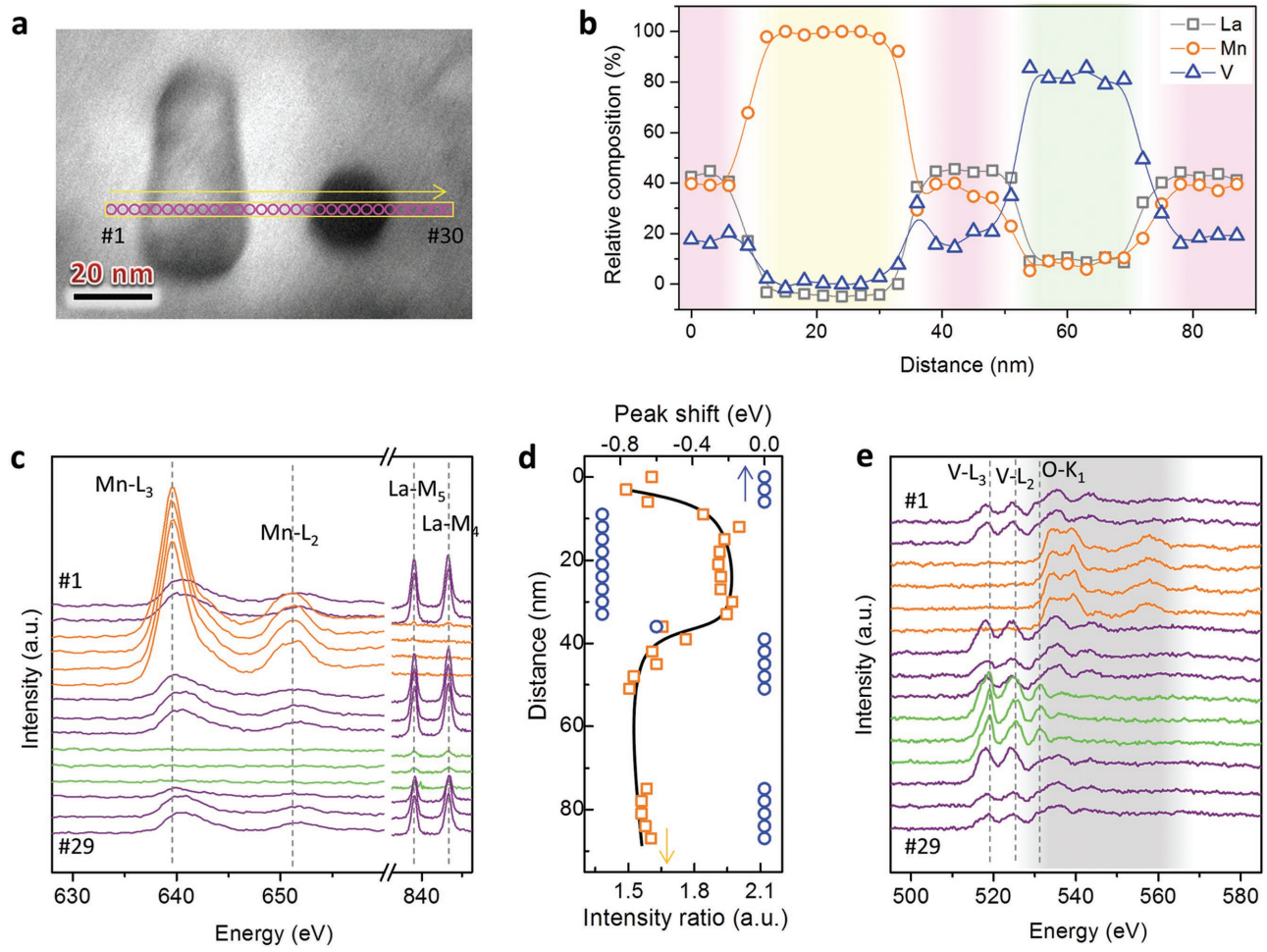

Figure 2. Chemical and electronic structures of nanostructured thin films. a) STEM image of gray (MnO) and dark (V_2O_3) nanopillars. Electron energy loss spectroscopy (EELS) line-scan across both nanopillars was carried out. The scanning direction and distance are indicated. b) Relative composition extracted from EELS line-scan showing the matrix contains cations of La, Mn, and V, the gray nanopillar only contains Mn cation and dark nanopillar only has V cation. c) Selected spectrum of Mn–L edges in the MnO (gray) nanopillar. The La–M edges are plotted as reference because La–M edges are usually less sensitive to chemical environments. d) Mn–L3 peak shift and the intensity ratio of L3 peak to L2 peak. In the MnO nanopillar region, Mn–L3, 2 peaks shift to left ≈0.9 eV and the intensity ratio increases. e) The V–L edges and O–K edges. The position and fine structures of O–K edges are sensitive to the chemical bonding.

variation of EELS across the thin-film matrix, a gray and a dark nanopillar were acquired in **Figure 2**a. Since the signal of core-loss edges of Sr is too low and noisy for quantitative analysis[21] and oxygen element is everywhere in the film, only V–L, La–M, and Mn–L edges are analyzed for quantification. The relative compositions extracted from EELS line scan in Figure 2b show that the matrix contains cations of La, Mn, and V, the gray nanopillar only contains Mn cation, and the dark nanopillar only contains V cation. We find that concentrations of La and Mn have similar distribution within the matrix region, while the V concentration is lower (≈20%) in the matrix. In the gray nanopillar region, the V is barely observed. From the comparison, we can conclude that the minor amount of V in the matrix is well above the error, indicating the matrix is LSMVO with mixed cations.

In addition, the valence state of Mn in the gray nanopillar was analyzed from the selected spectra of Mn–L edges, as shown in Figure 2c. The La–M edges are plotted as ref. [27] because positions of La–M edges are usually less sensitive to chemical environments. The Mn $L_{2,3}$ peaks in the gray nanopillar shift slightly to left as compared to that in the LSMVO matrix. In Figure 2d, the Mn $L_{2,3}$ peaks shift to left by ≈0.9 eV and the intensity ratio of L_3 peak to L_2 peak increases in the gray nanopillar. Comparing these features with data reported in the literature,[28] we can confirm that the Mn has a valence of 2+, i.e., the gray nanopillar is MnO. The V–L edges and O–K edges in Figure 2e show that V $L_{2,3}$ peaks in the dark nanopillar shift to right compared to the LSMVO matrix, while the O–K peaks in the dark nanopillar shift to left compared with LSMVO matrix and MnO nanopillar. The position and fine structures of O–K edges are sensitive to the chemical bonding.[29,30] By comparing the peak positions of V–L edges and O–K edges,[28] we can confirm that the dark nanopillar is V_2O_3. In addition, the appearance of V–L edges in the matrix also confirms the existence of V element. These results indicate that the target materials of LSMO and V_2O_3 react with each other during the deposition, resulting in the formation of a mixture of LSMVO matrix, MnO, and V_2O_3 nanopillars.

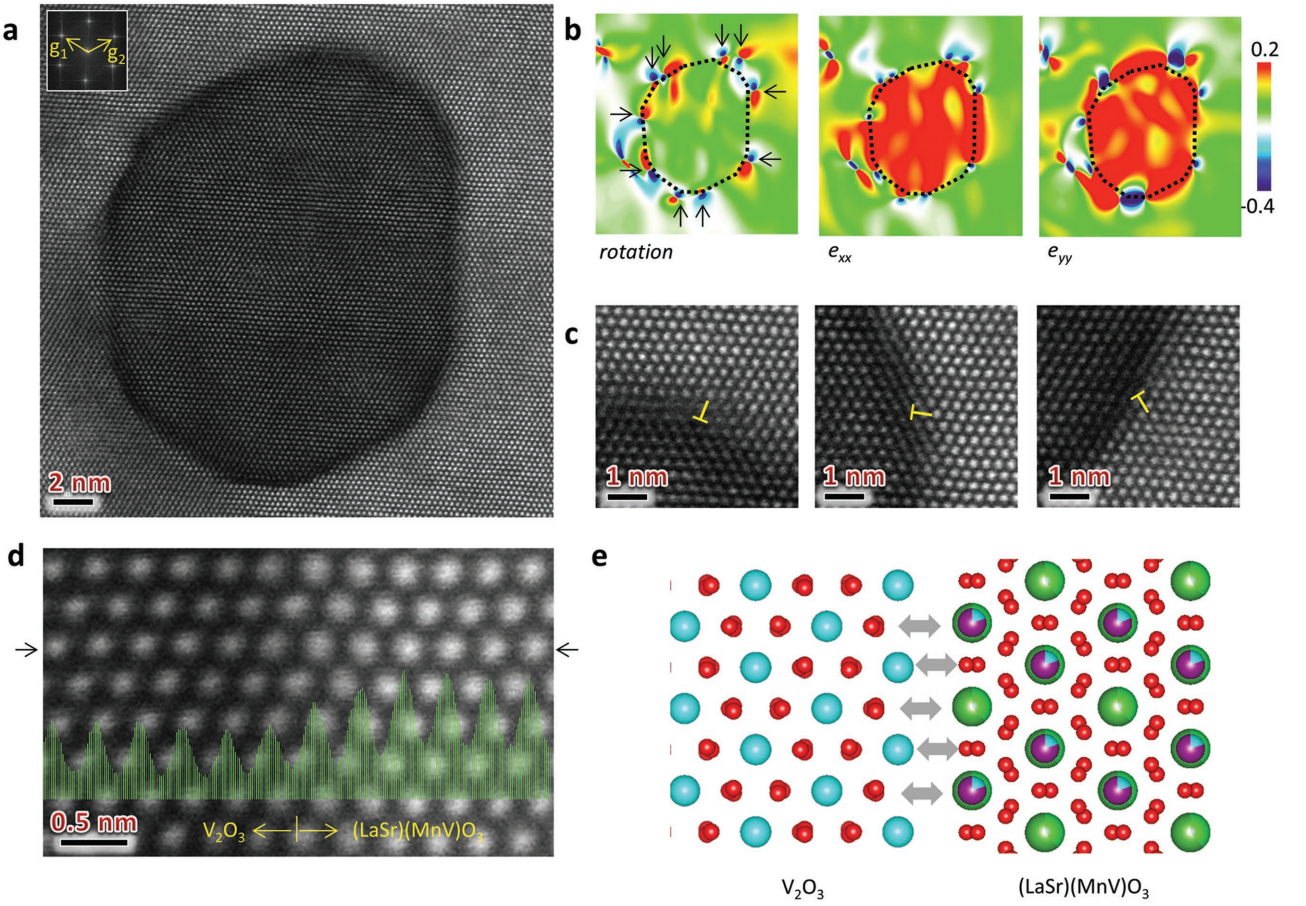

Figure 3. Atomic structure of V_2O_3 nanopillar. a) High-resolution high-angle annular dark filed (HAADF) image of V_2O_3 nanopillar (with darker contrast Z-contrast image) in the (LaSr)(MnV)O_3 matrix. Inset: FFT pattern. b) The strain and lattice rotation mappings calculated by Geometric phase analysis. The strain mapping showing the lattice distance in the nanopillar is (≈2%) larger than that of the matrix. The lattice rotation mapping showing the lattice orientation matches each other very well. The diffraction vectors are indicated in (a). The arrows in the lattice rotation mapping highlight the dislocation cores. c) Enlarged view of selected misfit dislocations at the interface of V_2O_3 nanopillar and matrix. d) Enlarged view of the interface showing the epitaxial relation. The intensity profile from the third row of atoms columns indicated by arrows determinates the position of interface. e) Atomistic model showing the bonding between V_2O_3 nanopillar and (LaSr)(MnV)O_3 matrix.

Atomically resolved HAADF images are used to determine the bonding at interface between the matrix and nanopillars. **Figure 3**a shows a representative atomically resolved planar view HAADF image of a V_2O_3 nanopillar (with darker contrast in the Z-contrast image) embedded in the LSMVO matrix. It can be seen that V_2O_3 nanopillar has the same orientation with the LSMVO matrix. The inset of fast Fourier transform (FFT) pattern in Figure 3a shows that the incident electron beam is along the [111] zone axis of LSMVO matrix, and the orientation relationship between the V_2O_3 nanopillar and the LSMVO matrix is (111)-V_2O_3//(111)-LSMVO. The lattice rotation mapping from geometric phase analysis (GPA)[31] in Figure 3b also shows that the lattice orientation matches each other very well. However, the misfit dislocations are also observed at the interface due to the lattice mismatch. These dislocations are visible in lattice rotation map (highlighted by the arrows) in Figure 3b. There is 4% lattice mismatch in *c* direction between LSMO and V_2O_3.[21] The GPA in Figure 3b clearly shows the (≈2%) strain across the interface of LSMVO matrix and V_2O_3 nanopillar, indicating a part of strain is relaxed at the interface due to the formation of dislocations. Figure 3c presents the enlarged views of selected misfit dislocations at the interface of the V_2O_3 nanopillar and LSMVO matrix. Except a few of edge dislocations, in the rest of regions the V_2O_3 nanopillar is perfectly bonded with the LSMVO matrix as shown in Figure 3d, in which the position of interface is determined by the intensity profile in the Z-contrast image. On the basis of these results above, an atomistic model of the bonding between V_2O_3 nanopillar and LSMVO matrix is proposed and shown in Figure 3e.

Unlike V_2O_3 nanopillar, the MnO nanopillar is incoherent with the LSMVO matrix due to the large dissimilarity in structure, as shown in the atomically resolved HAADF image from a plan-view specimen in **Figure 4**a. The corresponding FFT pattern in Figure 4b also shows that the lattice of the MnO nanopillar does not match the LSMVO matrix. The enlarged images from the square regions in Figure 4a labeled with purple and orange outlines show the atomic structures of the LSMVO matrix and the MnO nanopillar in Figure 4c,d, respectively. The LSMVO matrix still displays perfect atomic arrangements with the viewing direction of [111] zone axis. However, only the

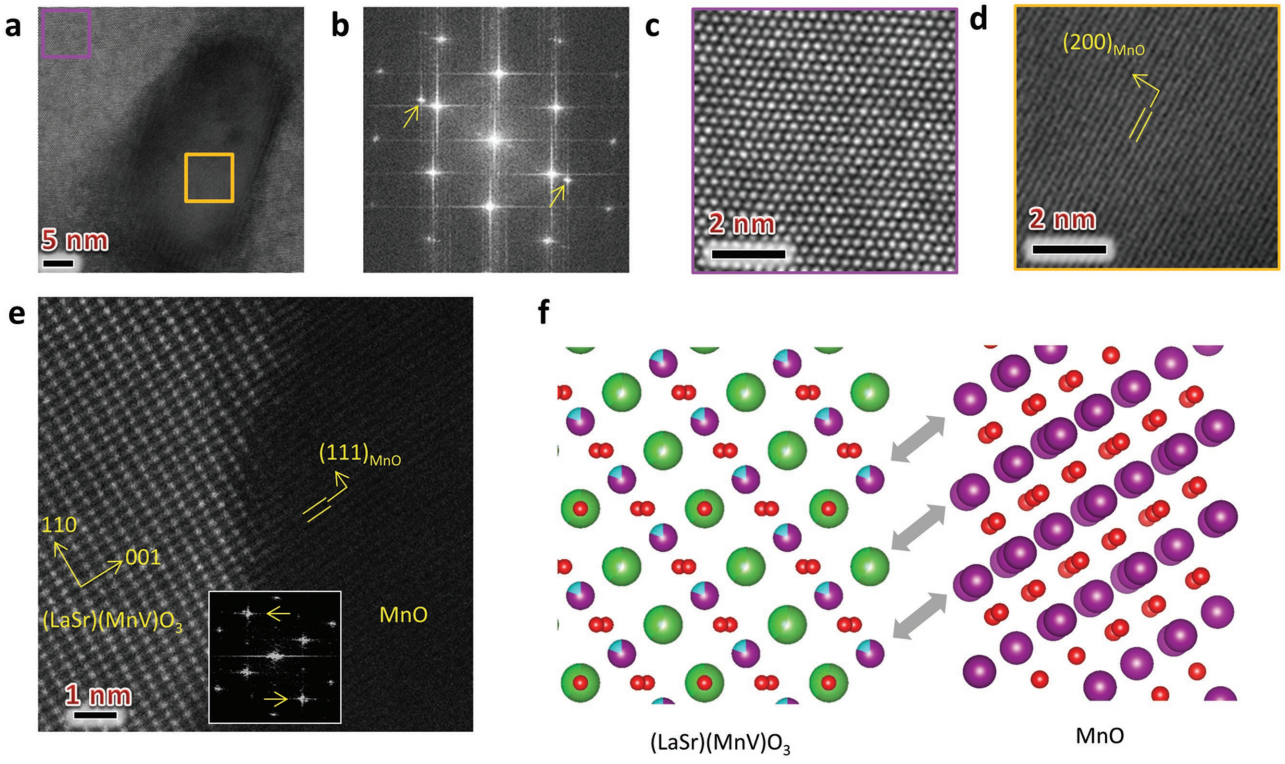

Figure 4. Atomic structure of MnO nanopillar. a) High-resolution HAADF image of MnO nanopillar from a planar view nanostructured thin film. b) The corresponding FFT pattern showing the lattice of nanopillar does not match the matrix. c) Enlarged view of square region in the matrix showing the viewing direction is [111]. d) Enlarged view of square region in the MnO nanopillar. (200) lattice fringes are observed. e) Cross-sectional high-resolution HAADF image of the boundary between MnO nanopillar and $(LaSr)(MnV)O_3$ matrix showing [111] of nanopillar matches [110] of matrix. f) Atomistic model showing the bonding between MnO nanopillar and $(LaSr)(MnV)O_3$ matrix.

(200) lattice planes can be seen in the MnO nanopillar. Therefore, there is no clear orientation relation between the MnO nanopillar and LSMVO matrix from the planar view image. The atomically resolved cross-sectional HAADF image of the phase boundary between MnO nanopillar and LSMVO matrix is also analyzed in Figure 4e. It shows that the (111) planes of nanopillar match the (110) planes of matrix. The inset of corresponding FFT pattern in Figure 4e indicates that the orientation relationship between the MnO nanopillar and the LSMVO matrix is (111)-MnO//(110)-LSMVO. Similarly, an atomistic model for the bonding between MnO nanopillar and LSMVO matrix is proposed in Figure 4f.

Based on the observed results, we can deduce that the target materials of LSMO and V_2O_3 react with each other during the deposition. A small amount of V ions substitute partial Mn ions, resulting in the formation of LSMVO matrix, i.e., LSMO + V_2O_3 → LSMVO + MnO. The detection of V in LSMO as occurring in our nanocomposite films is similar to the consequence of the Mn–Zr substitution[32–34] that the substitutional Zr occupies the Mn site in the LSMO matrix. On the other hand, the cationic exchange between LSMO and V_2O_3 also forms MnO nanopillars. Moreover, there is still some V_2O_3 that do not react with LSMO, leading to the formation of V_2O_3 nanopillars. The formation of nanopillar composite oxides depends on the LSMO and V_2O_3 ratio during growth.[21] The control of LSMO to V_2O_3 ratio during growth thus can leads to different nanocomposite structure and tunable metal–insulator transition. In addition, in respect of the distinctly different morphology of MnO and V_2O_3 nanopillars, the surface free energy and interfacial strain energy may play a central role since the MnO–LSMVO and V_2O_3–LSMVO interface structures are quite different as illustrated above. Further research should be conducted to investigate the underlying physics that gives rise to specific nanopillars shape and morphology.

We also investigate the interface bonding between LSMVO matrix and smaller size V_2O_3 nanopillars. Detailed results are shown in Figure S3 (Supporting Information). The lower density of misfit dislocations for the smaller size V_2O_3 nanopillar suggests the presence of size effects on the strain relaxation. The interface between V_2O_3 matrix and LSMVO nanopillars is also studied as shown in Figures S4 and S5 (Supporting Information). We find that the atomic bonding between LSMVO and V_2O_3 remains the same and misfit dislocations are also observed at the interface. In addition, despite large structural dissimilarity between LSMVO and MnO, they still find the most natural way to bond together, indicating the lattice plane match dominates the bonding at the heterointerfaces in these transition metal oxides.

3. Conclusions

In summary, the atomic structure and chemistry of the LSMVO matrix with MnO and V_2O_3 nanopillars are studied

by using atomically resolved STEM and EELS. We find that the LSMVO thin-film matrix is embedded with two self-assembled columnar nanocomposite oxides, i.e., MnO and V_2O_3 nanopillars. The size of MnO nanopillar is larger than that of V_2O_3 nanopillar. The LSMVO film matrix is epitaxially grown on the LAO substrate. The bonding between V_2O_3 nanopillars and LSMVO matrix is basically semicoherent (i.e., [111] V_2O_3//[111] LSMVO) with the strain being relaxed partially due to the formation of edge dislocations. In contrast, the bonding between MnO nanopillars and LSMVO matrix is incoherent. Only the (111) planes of MnO nanopillar match the (110) planes of LSMVO matrix. Our study reveals the atomic structure and chemistry of the nanosized phases in the composite thin films and identifies the atomic bonding at the heterointerfaces. In these transition metal oxides, the atomic bonding at the heterointerfaces is mainly governed by the lattice plane match. These findings provide useful information for understanding the structure-driven transport properties of these complex thin films. The atomic bonding information is also prerequisite for atomistic simulations of these heterostructures in future.

4. Experimental Section

The nanopillar composite films were deposited on $LaAlO_3$ (LAO) (111) substrates via alternate deposition by an ultrahigh vacuum PLD system using stoichiometric $La_{2/3}Sr_{1/3}MnO_3$ and V_2O_3 targets. A schematic view of the alternate growth of thin films is plotted in Figure 1a. The details of the growth process were reported elsewhere.[21] The deposition time ratio of LSMO to V_2O_3 was 1.3 and the total deposition time was about 80 min. The structures of the thin films were examined by X-ray diffraction (XRD) using Cu Kα radiation (λ = 1.5406 Å) and the XRD data were displayed in Figure S1 (Supporting Information), which is in good agreement with the transmission electron microscopy (TEM) data. The microstructures of the thin films were characterized by spherical aberration-corrected STEM (JOEL 2100F). The TEM specimens were prepared by the mechanical polishing followed by the argon ion milling (Precision Ion Polishing System, Gatan, Model 691). At the final stage of ion milling, the voltage was set at 0.3 kV for about 4 min to remove the surface amorphous layer and minimize the damage. The chemical compositions and electronic properties were extracted by conducting EELS mapping in the STEM mode with subangstrom spatial resolution and ≈0.7 eV energy resolution.

Supporting Information

Supporting Information is available from the Wiley Online Library or from the author.

Acknowledgements

The authors acknowledge the support from Prof. Xiaoqing Pan from University of Michigan and Prof. Jiandi Zhang and Prof. E. W. Plummer from Louisiana State University. Dr. X. M. Ma acknowledges Dr. X. J. Li in Peking University for the writing polishing. The work in Peking University was supported by from the National Basic Research Program of China (2016YFA0300804, 2016YFA0300903), the National Natural Science Foundation of China (51502007, 51672007), and "2011 Program" Peking-Tsinghua-IOP Collaborative Innovation Center of Quantum Matter. This work was partly supported by U.S. DOE under Grant No. DOE DE-SC0002136.

Conflict of Interest

The authors declare no conflict of interest.

Keywords

EELS, (LaSr)(MnV)O_3 thin films, nanocomposites oxides, nanopillars, STEM

Received: February 22, 2017
Revised: March 22, 2017
Published online: May 10, 2017

[1] J. Zhang, R. D. Averitt, *Annu. Rev. Mater. Res.* **2014**, *44*, 19.
[2] M. Uehara, S. Mori, C. H. Chen, S. W. Cheong, *Nature* **1999**, *399*, 560.
[3] C. H. Chen, S. W. Cheong, *Phys. Rev. Lett.* **1996**, *76*, 4042.
[4] A. Moreo, S. Yunoki, E. Dagotto, *Science* **1999**, *283*, 2034.
[5] M. Fath, S. Freisem, A. A. Menovsky, Y. Tomioka, J. Aarts, J. A. Mydosh, *Science* **1999**, *285*, 1540.
[6] K. Ueda, H. Tabata, T. Kawai, *Science* **1998**, *280*, 1064.
[7] A. Ohtomo, D. A. Muller, J. L. Grazul, H. Y. Hwang, *Nature* **2002**, *419*, 378.
[8] A. V. Boris, Y. Matiks, E. Benckiser, A. Frano, P. Popovich, V. Hinkov, P. Wochner, M. Castro-Colin, E. Detemple, V. K. Malik, C. Bernhard, T. Prokscha, A. Suter, Z. Salman, E. Morenzoni, G. Cristiani, H. U. Habermeier, B. Keimer, *Science* **2011**, *332*, 937.
[9] S. Middey, D. Meyers, M. Kareev, E. J. Moon, B. A. Gray, X. Liu, J. W. Freeland, J. Chakhalian, *Appl. Phys. Lett.* **2012**, *101*, 261602.
[10] H. Zheng, Q. Zhan, F. Zavaliche, M. Sherburne, F. Straub, M. P. Cruz, L. Q. Chen, U. Dahmen, R. Ramesh, *Nano Lett.* **2006**, *6*, 1401.
[11] J. L. MacManus-Driscoll, P. Zerrer, H. Wang, H. Yang, J. Yoon, A. Fouchet, R. Yu, M. G. Blamire, Q. Jia, *Nat. Mater.* **2008**, *7*, 314.
[12] H. Yang, H. Wang, J. Yoon, Y. Wang, M. Jain, D. M. Feldmann, P. C. Dowden, J. L. MacManus-Driscoll, Q. Jia, *Adv. Mater.* **2009**, *21*, 3794.
[13] R. Kapadia, Z. Fan, K. Takei, A. Javey, *Nano Energy* **2012**, *1*, 132.
[14] A. Imai, X. Cheng, H. L. Xin, E. A. Eliseev, A. N. Morozovska, S. V. Kalinin, R. Takahashi, M. Lippmaa, Y. Matsumoto, V. Nagarajan, *ACS Nano* **2013**, *7*, 11079.
[15] S. Cho, C. Yun, S. Tappertzhofen, A. Kursumovic, S. Lee, P. Lu, Q. Jia, M. Fan, J. Jian, H. Wang, S. Hofmann, J. L. MacManus-Driscoll, *Nat. Commun.* **2016**, *7*, 12373.
[16] X. Ning, Z. Wang, Z. Zhang, *Adv. Funct. Mater.* **2014**, *24*, 5393.
[17] H. Zheng, J. Wang, S. E. Lofland, Z. Ma, L. Mohaddes-Ardabili, T. Zhao, L. Salamanca-Riba, S. R. Shinde, S. B. Ogale, F. Bai, D. Viehland, Y. Jia, D. G. Schlom, M. Wuttig, A. Roytburd, R. Ramesh, *Science* **2004**, *303*, 661.
[18] S. A. Köster, V. Moshnyaga, K. Samwer, O. I. Lebedev, G. v. Tendeloo, O. Shapoval, A. Belenchuk, *Appl. Phys. Lett.* **2002**, *81*, 1648.
[19] V. Moshnyaga, B. Damaschke, O. Shapoval, A. Belenchuk, J. Faupel, O. I. Lebedev, J. Verbeeck, G. V. Tendeloo, M. Mücksch, V. Tsurkan, R. Tidecks, K. Samwer, *Nat. Mater.* **2003**, *2*, 247.
[20] A. Chen, Z. Bi, C. F. Tsai, J. Lee, Q. Su, X. Zhang, Q. Jia, J. L. MacManus-Driscoll, H. Wang, *Adv. Funct. Mater.* **2011**, *21*, 2423.
[21] Z. L. Liao, P. Gao, S. Stadler, R. Y. Jin, X. Q. Pan, E. W. Plummer, J. D. Zhang, *Appl. Phys. Lett.* **2013**, *103*, 043112.
[22] H. Y. Hwang, Y. Iwasa, M. Kawasaki, B. Keimer, N. Nagaosa, Y. Tokura, *Nat. Mater.* **2012**, *11*, 103.
[23] W. Zhang, R. Ramesh, J. L. MacManus-Driscoll, H. Wang, *MRS Bull.* **2015**, *40*, 736.

[24] H. J. Liu, V. T. Tra, Y. J. Chen, R. Huang, C. G. Duan, Y. H. Hsieh, H. J. Lin, J. Y. Lin, C. T. Chen, Y. Ikuhara, Y. H. Chu, *Adv. Mater.* **2013**, *25*, 4753.
[25] Y. Zhu, W. S. Chang, R. Yu, R. Liu, T. C. Wei, J. H. He, Y. H. Chu, Q. Zhan, *Appl. Phys. Lett.* **2015**, *107*, 191902.
[26] Y. Zhu, P. Liu, R. Yu, Y. H. Hsieh, D. Ke, Y. H. Chu, Q. Zhan, *Nanoscale* **2014**, *6*, 5126.
[27] A. B. Shah, Q. M. Ramasse, S. J. May, J. Kavich, J. G. Wen, X. Zhai, J. N. Eckstein, J. Freeland, A. Bhattacharya, J. M. Zuo, *Phys. Rev. B* **2010**, *82*, 115112.
[28] H. Tan, J. Verbeeck, A. Abakumov, G. V. Tendeloo, *Ultramicroscopy* **2012**, *116*, 24.
[29] D. A. Muller, N. Nakagawa, A. Ohtomo, J. L. Grazul, H. Y. Hwang, *Nature* **2004**, *430*, 657.
[30] P. Gao, Y. Zhang, S. Y. Zhang, S. Lee, J. Weiss, J. R. Jokisaari, E. E. Hellstrom, D. C. Larbalestie, C. B. Eom, X. Q. Pan, *Phys. Rev. B* **2015**, *91*, 104525.
[31] M. J. Hÿtch, E. Snoeck, R. Kilaas, *Ultramicroscopy* **1998**, *74*, 131.
[32] M. S. Kim, J. B. Yang, Q. Cai, W. J. James, W. B. Yelon, P. E. Parris, S. K. Malik, *J. Appl. Phys.* **2007**, *102*, 013531.
[33] D. Zhou, W. Sigle, E. Okunishi, Y. Wang, M. Kelsch, H. U. Habermeier, P. A. van Aken, *APL Mater.* **2014**, *2*, 127301.
[34] D. Zhou, W. Sigle, M. Kelsch, H. U. Habermeier, P. A. van Aken, *Adv. Mater. Interfaces* **2015**, *2*, 1500377.

